

Nanoparticle-Mediated Interface Engineering for Uniform, Reproducible Electron Transport Layers in Scalable Perovskite Solar Cells

Charlie Henderson, Adriano S. Marques, Izabela S. Bicalho, Lucy J. F. Hart, Amy Monahan, Katherine Stewart, Koki Asano, Tianhao Lan, Martin Vacha, Molly M. Stevens, Piers R. F. Barnes, Diego Bagnis, and Ji-Seon Kim*



Cite This: *ACS Appl. Mater. Interfaces* 2026, 18, 12738–12748



Read Online

ACCESS |



Metrics & More



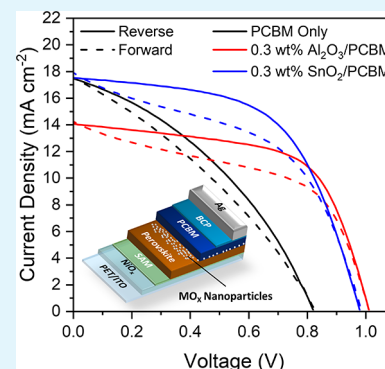
Article Recommendations



Supporting Information

ABSTRACT: As lab-scale perovskite solar cells (PSCs) approach their efficiency limits, reproducing this performance in large-area, manufacturable devices remains challenging. Here, we show that printing interlayers of metal oxide nanoparticles, specifically Al_2O_3 and SnO_2 , can systematically control the morphology and interfacial energetics of solution-processed PC_{61}BM electron transport layers (ETLs) in flexible roll-to-roll printed PSCs. These nanoparticle interlayers enhance ETL uniformity, reduce pinholes, and increase shunt resistance, improving power conversion efficiencies (PCEs) and reducing device failure rates by 50%. Through a combination of systematic device characterization, morphological, spectroscopic and energetic analysis, coupled with drift-diffusion simulations, the distinct roles of insulating (Al_2O_3) and semiconducting (SnO_2) nanoparticle interlayers in mediating carrier extraction and recombination are elucidated. Al_2O_3 suppresses interfacial recombination and improves device reproducibility, albeit with some penalty in short-circuit current, whereas SnO_2 enhances electronic coupling and charge extraction, delivering a champion PCE of 11.0% (active area: 0.5 cm^2). Incorporating SnO_2 interlayers into larger-area modules (active area: 7.2 cm^2) further demonstrates the robustness of this strategy under manufacturing-relevant conditions. Together, these results provide an important framework for nanoparticle-mediated interface engineering and establish a simple, effective, and scalable route to improving both performance and yield in printed large-area PSCs.

KEYWORDS: photovoltaics, perovskites, scalable processing, interface engineering, interfacial charge extraction



INTRODUCTION

The power conversion efficiency (PCE) of research scale metal halide perovskite (MHP) solar cells now exceeds 26%,¹ comparable to the best silicon based modules. However, significant challenges remain in reproducing this performance at scales relevant for power generation. Compared to traditional crystalline inorganic semiconductors, perovskites are more tolerant to mechanical deformation, making them attractive for continuous roll-to-roll (R2R) processing.^{2,3}

Perovskite films can be formed by either solution processing, where a wet film containing the precursor materials is coated onto a substrate, or by evaporation, where precursor materials are evaporated under ultrahigh vacuum onto a substrate where the perovskite forms.⁴ Both are methods are being targeted for industrial scale up, however, to the best of our knowledge, only solution processing has been successfully demonstrated in a continuous R2R process.⁵ High capital expenditure to procure equipment and the relatively early stage of evaporated perovskite research (as compared to solution processing) currently makes this technique less attractive to industry. In this work we focus on solution processed perovskite solar cells.

Presently, most MHP research is focused on spin-casting films which, in an academic laboratory, is a simple process resulting in high quality, reproducible films. However, substrate size constraints, high material wastage, and incompatibility with continuous processing makes spin coating unattractive for commercial scale up.

Sequential printing of the required device layers is a significant challenge for upscaling as methods used for small, spin coated devices often do not translate directly to meniscus assisted techniques such as blade or slot-die coating.⁶ An example is the printing of PC_{61}BM electron transport layers. PC_{61}BM coating on perovskite is facile using a spin coater and rarely requires extensive optimization for regular Pb based perovskites. However, when moving to larger areas using blade

Received: December 2, 2025

Revised: February 3, 2026

Accepted: February 9, 2026

Published: February 18, 2026



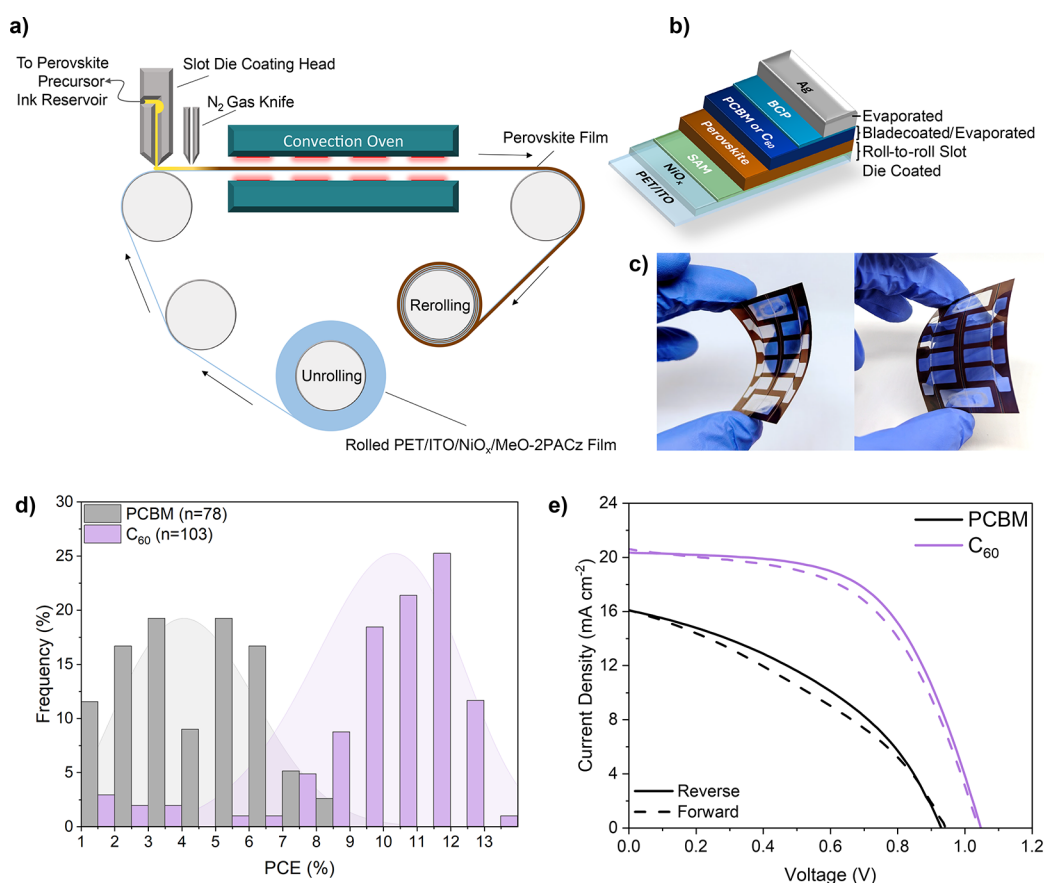


Figure 1. (a) Simplified diagram of the roll-to-roll printing process used to produce the perovskite films in this work; (b) reference device stack; (c) photographs showing example flexible devices; (d) histogram showing the PCE distributions of PSCs utilizing PC₆₁BM (black) and C₆₀ (purple) ETLs (devices with PCE < 1% excluded); and (e) example JV curves of the PSCs shown in Figure 1d.

or slot-die coating, preventing pinhole formation and dewetting becomes a significant challenge.⁷

The deposition of high-quality blade coated perovskite films can be assisted by depositing noncontinuous metal oxide nanoparticle seeding layers. The nanoparticles seed the crystallization of a uniform perovskite film on top of hole transport materials (HTMs) with poor wettability in both spin, blade, and spray coated devices.^{8–11} Recent work by Jin et al. demonstrated that the quality of spin-cast PC₆₁BM films deposited on Sn–Pb narrow band gap perovskite was improved by prior application of a thin layer of spin-cast Al₂O₃ nanoparticles on the perovskite surface.¹² They found that this layer enabled the PC₆₁BM to conformally coat the perovskite surface, reducing shunts and improving device performance. Uddin et al. and Li et al. have also previously demonstrated that additives in the PC₆₁BM solution result in improved performance in blade coated perovskite devices.^{7,13}

The goal of this work is to improve the printing of fullerene electron transport layers (ETLs) from solution, toward full R2R solution processing of perovskite solar cells. To this end we apply blade coated nanoparticle layers of two metal oxides, alumina (Al₂O₃) and tin oxide (SnO₂), between the perovskite and PC₆₁BM. The former is an electronic insulator, while the latter is an n-type semiconductor. Both result in improved uniformity of the PC₆₁BM film, increasing the reproducibility and performance of the fabricated solar cells. We investigate the impact of nanoparticle type on the modification of the perovskite/PC₆₁BM interface, demonstrating that nanoparticle electronic structure plays a key role in governing interfacial

charge transfer. Finally, we demonstrate the utility of this approach for the fabrication of large area devices by applying SnO₂ nanoparticles in minimodules.

RESULTS AND DISCUSSION

Comparison of Evaporated and Solution-Processed Electron Transport Layers

Typical p-i-n perovskite solar cells incorporate fullerene-based electron transport layers, usually evaporated C₆₀ or solution processed phenyl-C₆₁-butyric acid methyl ester (PC₆₁BM). We fabricated flexible p-i-n devices with the structure: polyethylene terephthalate (PET)/ITO/NiO_x/MeO-2PACz/perovskite/fullerene/bathocuproine (BCP)/Ag, where ‘fullerene’ is either solution processed PC₆₁BM or evaporated C₆₀. In all devices the NiO_x, MeO-2PACz and perovskite layers were deposited sequentially via slot die coating in a roll-to-roll process outlined in Figure 1a.¹⁴ The PC₆₁BM/BCP layers were deposited sequentially by blade coating and the C₆₀/BCP layers were deposited sequentially by thermal evaporation. All devices had thermally evaporated Ag cathodes. All printed layers were processed in ambient air in a cleanroom environment.

Devices with blade coated PC₆₁BM ETLs exhibited exceptionally low performance and poor reproducibility compared to devices with evaporated C₆₀ ETLs (Figure 1d,e). The performance drop in the PC₆₁BM devices is driven by reductions in the open circuit photovoltage (V_{OC}), the fill factor (FF) and short circuit photocurrent density (J_{SC}), with the shunt and series resistance (R_{shunt} and R_{series}) also

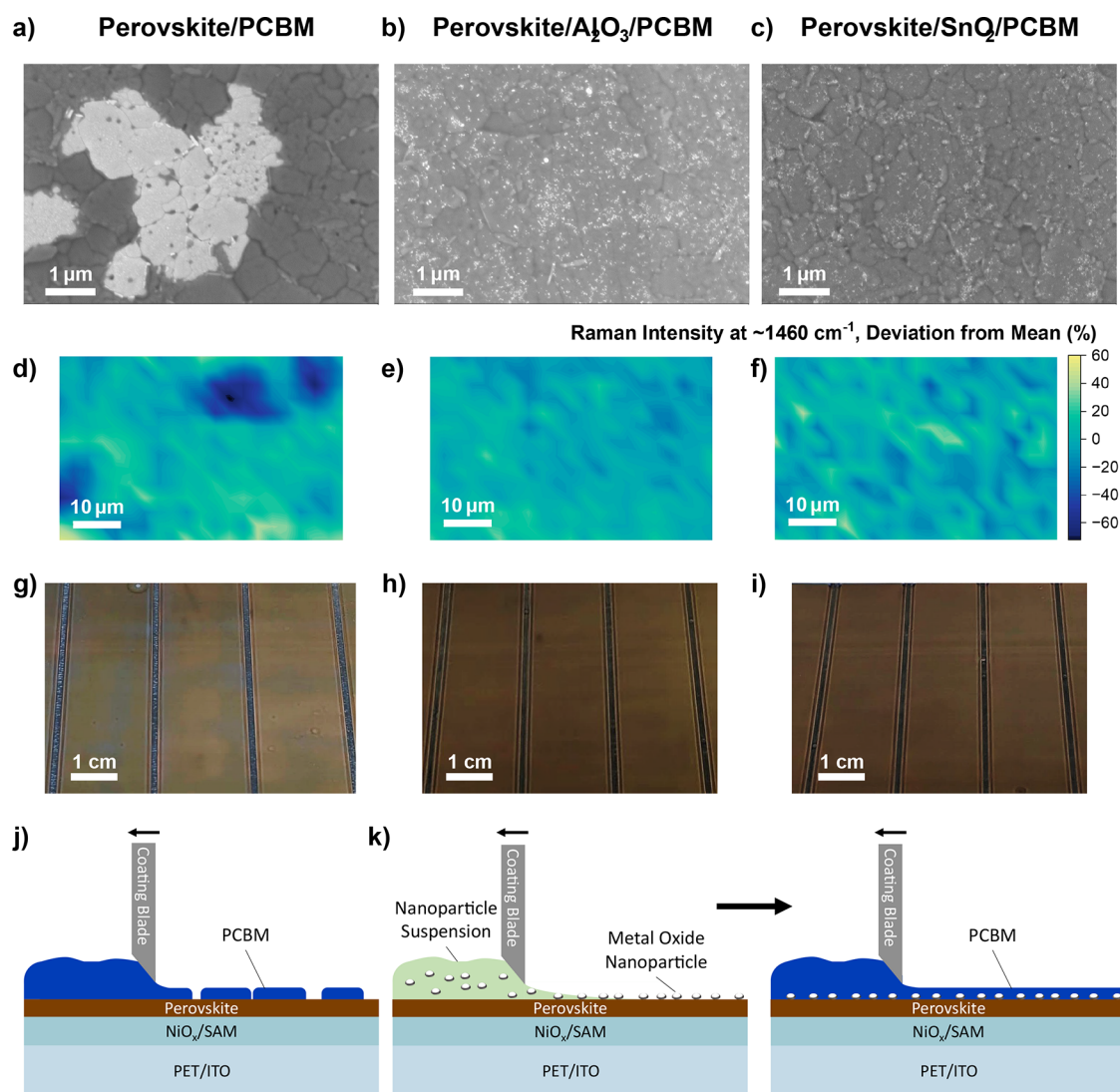


Figure 2. Impact of nanoparticles on the morphology of printed PC₆₁BM films. All images were collected on films with the base structure of PET/NiO_x/Me-2PACz/Perovskite. (a–c) SEM images of Perovskite/PC₆₁BM, Perovskite/Al₂O₃ NPs/PC₆₁BM, and Perovskite/SnO₂ NPs/PC₆₁BM films. (d–f) Maps of the intensity of the characteristic PC₆₁BM Raman peak at ~1460 cm⁻¹ of Perovskite/PC₆₁BM, Perovskite/Al₂O₃ NPs/PC₆₁BM, and Perovskite/SnO₂ NPs/PC₆₁BM films. (g–i) Photographs of Perovskite/PC₆₁BM, Perovskite/Al₂O₃ NPs/PC₆₁BM, and Perovskite/SnO₂ NPs/PC₆₁BM films. Diagrams outlining the impact on PC₆₁BM film coating without (j) and with (k) a metal oxide nanoparticle interlayer.

decreasing and increasing respectively (Figure S1, Table S1). Of the 136 reference PC₆₁BM devices fabricated for this study, 38% had PCEs below 1% (our threshold for a ‘failed’ device), compared to just 4% of the C₆₀ based devices.

PC₆₁BM Film Formation Dictated by the Presence of Nanoparticle Interlayers

A recent report by Jin et al. showed that inserting a discontinuous, spin-coated Al₂O₃ nanoparticle interlayer between mixed Sn/Pb perovskites and PC₆₁BM improves PC₆₁BM coverage and device performance.¹² However, printed metal-oxide nanoparticle interlayers for flexible, roll-to-roll perovskite solar cells remain unaddressed. Here, we transform this concept to scalable processing.

We blade coated both insulating Al₂O₃ and n-type semiconducting SnO₂ nanoparticles at a range of concentrations in isopropyl alcohol (IPA) followed sequentially by the PC₆₁BM layer in o-xylene. o-Xylene was selected due to its significantly lower toxicity compared to chlorobenzene, the most common solvent used for PC₆₁BM processing in PSCs.

The reduced toxicity makes o-xylene more attractive for scale up manufacturing due to significantly reduced work place exposure limits.^{15,16}

The Al₂O₃ and SnO₂ nanoparticles form a noncontinuous layer on the perovskite, with the device optimized concentration of 0.3 wt % resulting in approximately 20% surface coverage of the perovskite film as quantified by scanning electron microscopy (SEM) (Figures S2 and S3). The SEM also demonstrates the functional difference between the insulating Al₂O₃ and the semiconducting SnO₂. The increased brightness of the Al₂O₃ nanoparticles compared to the SnO₂ nanoparticles is a result of charging of the Al₂O₃ nanoparticles by incident electrons from the field emission gun. Due to the insulating nature of Al₂O₃, incident electrons accumulate in the nanoparticles, leading to scattering of successive incident electrons.¹⁷ In contrast, the SnO₂ particles remain similarly bright as the underlying perovskite due to their semiconducting nature allowing them to redistribute charge to the perovskite surface and subsequently to ground.

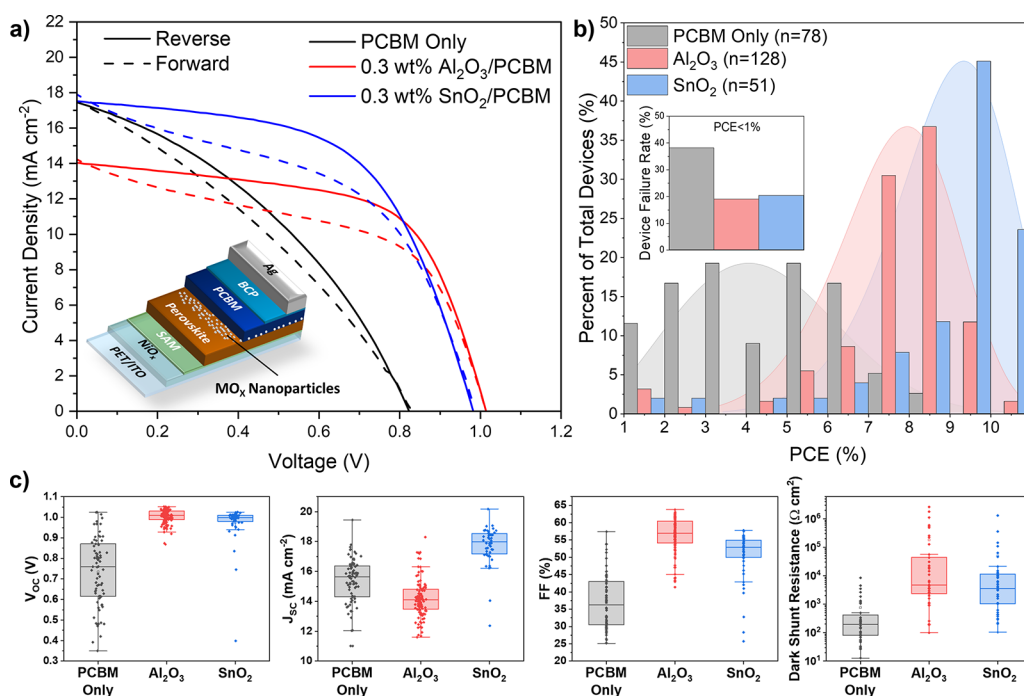


Figure 3. Impact of metal oxide nanoparticle interlayers on device performance. (a) JV curves of representative devices with and without 0.3 wt % nanoparticle interlayers. The inset diagram shows the complete device structure. (b) Histogram showing the PCE distribution of optimized devices with PCE \geq 1%. The inset chart shows the percentage of devices of each type with PCE < 1%. (c) Statistics of selected performance parameters for each optimized device type.

The impact of nanoparticles on PC₆₁BM film formation is shown in Figure 2. SEM images of the reference perovskite/PC₆₁BM films have large bright areas which are several microns across; image analysis shows these regions cover approximately 7% of the total film (Figure S4). We note that these areas show the morphology of the underlying perovskite film more clearly and with a higher brightness. In contrast both the Al₂O₃ and SnO₂ modified films are more uniform under SEM, with no large bright regions. Further SEM images of the films at different magnifications are shown in Figure S5. To understand the chemical makeup of these regions we applied Raman mapping (Figures 2d–f and S6). By mapping the intensity of the characteristic PC₆₁BM peak at 1465 cm⁻¹ we find that the bright areas in the SEM image are vacancies in the PC₆₁BM film.^{18,19} In contrast, the nanoparticle/PC₆₁BM films have no vacancies visible in either the SEM images or Raman maps. The effect of these vacancies is evident to the naked eye, with the PC₆₁BM only films appearing lighter in color, less uniform and slightly cloudy compared to the nanoparticle/PC₆₁BM films which are uniformly the characteristic brown color of PC₆₁BM (Figure 2g–i).

The surface morphology of the films was investigated using atomic force microscopy (AFM) (Figure S7). Unlike the work of Jin et al. we saw no significant change in the roughness of either the perovskite or perovskite/PC₆₁BM films with and without nanoparticles present.¹² This suggests that the roughness of the surface of the perovskite films is not the cause of the poor coating of PC₆₁BM on the reference perovskite films.

Impact of Metal Oxide Nanoparticle Interlayers on PSC Performance

To understand the impact of the improved PC₆₁BM film morphology we applied the nanoparticle interlayers in PSCs of the structure (PET)/ITO/NiO_x/MeO-2PACz/perovskite/

Metal Oxide Nanoparticles/PC₆₁BM/BCP/Ag. The results of the optimized concentration (0.3 wt % Al₂O₃ or SnO₂ in IPA) are summarized in Figure 3.

Upon addition of Al₂O₃ nanoparticles we observe an increase in the PCE, FF, and R_{shunt} as well as a significant reduction in device-to-device V_{OC} variation. Additionally, we observe a substantial reduction in the proportion of failed devices (PCE < 1%) from 38% in the reference devices to less than 18% in the Al₂O₃ modified devices. Results of experiments to optimize the coating parameters and concentration of the Al₂O₃ nanoparticle suspension are shown in Figure S8. As the concentration of the Al₂O₃ solution increases from 0.15 wt % to the optimum 0.3 wt % we observe an increase in device PCE, FF, V_{OC} and R_{shunt} . The addition of Al₂O₃ also results in decrease in device J_{SC} from an average of 15.3 ± 1.5 mA cm⁻² in the reference devices to 14.0 ± 1.7 mA cm⁻² in the optimized Al₂O₃ devices (Table S1). As the Al₂O₃ interlayer is noncontinuous (Figure S2), by increasing the concentration of the Al₂O₃ solution we are increasing the surface coverage of the nanoparticles. Al₂O₃ is an insulator which is not expected to mediate charge extraction from the perovskite,^{20,21} and therefore the decreased current in the devices with increased Al₂O₃ concentration may suggest that the Al₂O₃ nanoparticles block efficient charge extraction from the perovskite to the PC₆₁BM ETL. This is confirmed by the presence of significant ‘s-shape’ kink in the JV of the devices with a 0.62 wt % Al₂O₃ interlayer (Figure S8), which is indicative of an extraction barrier at the ETL resulting in an imbalance of electron and hole extraction rates.^{22–24}

To explore the effect of the electronic properties of the metal oxide nanoparticles on device performance we replaced the Al₂O₃ nanoparticle interlayer with SnO₂ nanoparticles. SnO₂ is an n-type semiconductor which is commonly applied as an ETM in perovskite solar cells.²⁵ Figure 3 compares the device

performance characteristics of devices incorporating blade coated layers of Al_2O_3 or SnO_2 nanoparticles deposited from a 0.3 wt % solution. An increase in mean J_{SC} values of the SnO_2 devices ($17.8 \pm 1.2 \text{ mA cm}^{-2}$) versus the reference and Al_2O_3 devices is observed, with minimal losses in both FF and V_{OC} . This leads to a significant increase in mean device PCE, with SnO_2 based devices achieving $8.95 \pm 1.87\%$ PCE, compared to $7.64 \pm 1.65\%$ for the Al_2O_3 -based devices and $4.39 \pm 1.90\%$ for the PC_{61}BM only reference devices (Table S1). Additionally, the proportion of failed devices (PCE < 1%) is unchanged when Al_2O_3 is replaced with SnO_2 , although device to device variation is slightly increased. The performance of the SnO_2 based devices is less dependent on the nanoparticle concentration compared to the Al_2O_3 -based devices (Figure S9). As the concentration of SnO_2 nanoparticles increases from 0.15 wt % there is an increase in V_{OC} , J_{SC} and FF. Both V_{OC} and FF reach their maximum values at 0.3 wt % of SnO_2 (the same concentration as for the Al_2O_3). However, the J_{SC} of the devices increases steadily to a maximum of $19.9 \pm 0.8 \text{ mA cm}^{-2}$ at the maximum tested concentration of 1.85 wt %. This suggests that, unlike the Al_2O_3 , the SnO_2 is active in extracting charges from the perovskite. Despite this high current, the drop in FF and V_{OC} at high SnO_2 concentrations means that the devices with the highest efficiency are fabricated using 0.3 wt % of SnO_2 .

The performance of PC_{61}BM only devices are limited by low shunt resistances, with most devices exhibiting shunt resistances below $1000 \Omega \text{ cm}^2$ with a median value of $194 \Omega \text{ cm}^2$ (Figure 3c). In contrast the median dark shunt resistances for devices with optimized Al_2O_3 and SnO_2 interlayers are 4803 and $3605 \Omega \text{ cm}^2$ respectively. This observation is consistent with the large vacancies in the PC_{61}BM film observed in the SEM images. By preventing the formation of these vacancies, the Al_2O_3 and SnO_2 nanoparticle interlayers prevent direct contact between the perovskite and the Ag cathode – increasing the shunt resistance and therefore device performance.

To assess the stability of the devices under study, encapsulated Al_2O_3 and SnO_2 nanoparticle modified devices were exposed to 1 Sun illumination in air under maximum power point tracking. The Al_2O_3 and SnO_2 devices exhibited T_{80} of 112 and 400 h respectively (Figure S10).

We finally confirmed that the improvements in device performance described are a result of the presence of the metal oxide nanoparticles, and not because of the IPA solvent they are suspended in. We fabricated devices which were treated with an IPA ‘rinse’, where neat IPA was blade coated across the perovskite prior to PC_{61}BM deposition using the same coating parameters as for the nanoparticles. We observed no difference in the performance of the reference devices and those treated with IPA, confirming that is the presence of the metal oxide nanoparticles, not their method of deposition, which is responsible for the observed improvement in performance (Figure S11).

Role of Nanoparticles in Charge Carrier Recombination and Extraction

External quantum efficiency (EQE) spectra of the reference and optimized nanoparticle interlayer devices are shown in Figure S12. All devices have a similar response onset, with band gap analysis (Figure S13) confirming a photovoltaic bandgap of 1.58 eV.^{26,27} Integrating the EQE spectra to find the total current produced by the devices gives the same trend

as the J_{SC} under 1 Sun illumination. By normalizing the spectra to their intensity at 400 nm the shape of the EQE responses can be compared. The normalized EQE response of both the Al_2O_3 and SnO_2 devices are very similar in shape, suggesting that the difference in current between the Al_2O_3 and SnO_2 devices is due to more efficient extraction of photogenerated charges in the SnO_2 device. The shape of the reference PC_{61}BM EQE spectrum is also similar to the nanoparticle modified devices at wavelengths <530 nm; however, at longer wavelengths a significant relative reduction in EQE is observed. Optical absorption depth in perovskite films is wavelength dependent, with short wavelength photons more likely to be absorbed close to the film’s surface and longer wavelength photons absorbed deeper into the film (i.e., closer to the perovskite/ETL interface).^{28,29} The reference device’s reduced EQE in the longer wavelength region is therefore consistent with increased recombination of photogenerated charges deeper in the film. Due to the incomplete coverage of the PC_{61}BM film, this is likely caused by direct contact between the perovskite and the Ag cathode.

We applied photoluminescence (PL) microscopy to partial device stacks (without BCP or Ag) to understand the nanoscale photophysical properties of the films, and local charge extraction and recombination phenomena. Spatially mapping the PL intensity and spectra of the perovskite/ PC_{61}BM only film reveals wide distribution in PL intensity (Figure S14). This is consistent with the incomplete surface coverage of the perovskite in the PC_{61}BM only sample leading to a reduction in PC_{61}BM /perovskite interfacial area and consequently less surface recombination/PL quenching. Addition of the nanoparticle interlayers reduces both the baseline intensity and spatial heterogeneity of the PL spectra, consistent with more complete surface coverage of the perovskite by the electron extraction layers - resulting in greater quenching of PL. The distribution of the PL peak positions (likely a result of local differences in halide composition in the perovskite) is unchanged by addition of the nanoparticle interlayers and the ETL. This confirms that the observations are a result of variation in interfacial charge extraction efficiency, rather than perovskite composition.

Transient PL decays of perovskite/ PC_{61}BM samples with and without nanoparticle modification are given in Figure S15a. All three samples show a similar fast decay at early times ($\tau_1 \approx 1 \text{ ns}$), followed by a slower decay at longer times (τ_2), as summarized in Figure S15b. The τ_2 decay is shortest for the SnO_2 nanoparticle modified sample (22.9 ns at $5 \times 10^5 \text{ Hz}$ laser repetition rate) followed by the Al_2O_3 modified sample (25.0 ns) then the reference PC_{61}BM only sample (26.2 ns). When interpreting the PL decay of perovskite films in contact with charge transport layers, the slower decay component (τ_2) is typically associated with the lifetime of carriers that are not rapidly trapped or recombined at the interface and can therefore be quenched by charge transfer to the fullerene layer.³⁰ Here we interpret the faster decays in the SnO_2 samples as evidence for faster, more efficient, extraction of charges – consistent with the broader set of data presented. The slower decay in the reference sample is likely due to the incomplete coverage of the perovskite by the PC_{61}BM resulting in reduced quenching of the PL. Importantly these differences in decay rate are independent of the repetition rate of the laser used, suggesting that the relative extraction rates are unaffected by state filling or carrier density.^{31,32} We also note that as the samples were illuminated through the PC_{61}BM (meaning

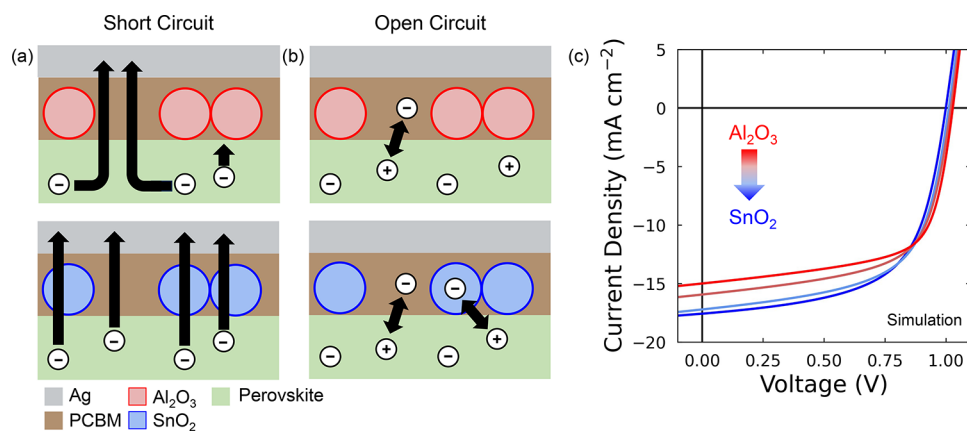


Figure 4. Results of Driftdiffusion calculations on the devices under study. Schematic diagrams of electron extraction processes at (a) J_{SC} and (b) V_{OC} of Al_2O_3 (top) and SnO_2 (bottom) nanoparticle-modified devices; (c) simulated JV curves illustrating four scenarios: reduced mobility near the ETL interface and lower electron recombination current at the interface (Al_2O_3 case, red), increased mobility and higher recombination current at the interface (SnO_2 case, blue), and two intermediate conditions between these two cases.

generation will occur close to the perovskite/ETL interface) the influence of carrier diffusion through the bulk perovskite upon the PL lifetimes will be minimal.³⁰

To better understand the effect of the nanoparticles on charge extraction and recombination, we model the devices' JV curves using Driftdiffusion,³³ a drift-diffusion software designed to simulate ordered semiconductor devices containing mobile ionic charge. Details of the simulation parameters are given in Tables S2 and S3 and the protocol is given in the Methods section. We note here that the HTL/perovskite interface was treated as Schottky diode due to the highly doped nature of the NiO ^{34,35} and to simplify the description of the device stack such that we can focus solely upon how changes in the ETL's properties affect the JV parameters. As Driftdiffusion only considers one spatial dimension, we cannot explicitly model the different nanoparticles due to their nonuniform spatial distributions across the perovskite surface (see Figure S2). However, by considering how their presence would alter the rates of extraction and recombination at the perovskite/ $PC_{61}BM$ interface, we can describe their effects by changing only two of the model's parameters: the perovskite's mobility and the surface recombination velocity of electrons at the perovskite/ $PC_{61}BM$ interface.

To understand why this is the case, we refer to Figure 4. Under short circuit conditions (Figure 4a), the Al_2O_3 nanoparticles prevent the transfer of electrons from the perovskite to the $PC_{61}BM$ due to their insulating nature. Thus, to be extracted, electrons must diffuse around the Al_2O_3 nanoparticles until they reach a region where the perovskite and $PC_{61}BM$ are in direct contact.²¹ The same is not true when SnO_2 nanoparticles are added since SnO_2 is electronically conductive. Consequently, electrons in the devices containing the Al_2O_3 nanoparticles will spend longer in the region of the perovskite near the perovskite/ $PC_{61}BM$ interface than they would in the devices with the SnO_2 nanoparticles. We can include this effect in our simulations by lowering the mobility of electronic carriers in the region of the perovskite close to the perovskite/ $PC_{61}BM$ interface. We stress that this lower mobility near the perovskite/ETL interface should be understood as an effective mobility, which decreases due to the fact electronic carriers must move laterally as well as in the direction parallel to the field to be extracted. As the effective mobility in this region decreases, electrons accumulate in the

perovskite bulk and these accumulated electrons undergo trap assisted recombination. This results in a lower J_{SC} , as is evident from the simulated JV curves shown in Figure 4c and matches closely the experimental data.

Considering now open circuit conditions (Figure 4b), here we propose that the presence of the electronically insulating Al_2O_3 nanoparticles reduces the fraction of the perovskite/ $PC_{61}BM$ interface across which there can be interfacial recombination (i.e., recombination of a perovskite hole with an ETL electron) when compared to the case of the SnO_2 nanoparticles.²¹ This difference can be included in our simulations by lowering the surface recombination velocity of electrons at the perovskite/ $PC_{61}BM$ interface. As shown in Figure 4c, changing this parameter recreates a shift in V_{OC} comparable to that observed experimentally.

To further explore the impact of the different nanoparticles we performed surface photovoltage (SPV) measurements using a Kelvin probe and white light source. We measured the SPV of partial device stacks consisting of PET/ITO/HTL/Perovskite/ $PC_{61}BM$, with and without nanoparticle interface modification. The results of these measurements (Figure 5) show distinct differences in the turn-on and turn-off responses of the different samples. The positive SPV response under illumination indicates the accumulation of an excess of

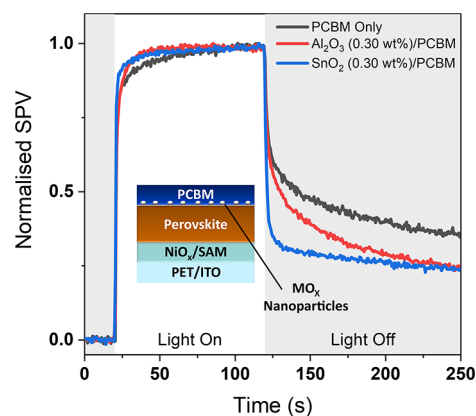


Figure 5. Normalized surface photovoltage responses of reference (black), Al_2O_3 (red), and SnO_2 (blue) nanoparticle-modified partial device stacks under white light illumination (1/5 Sun).

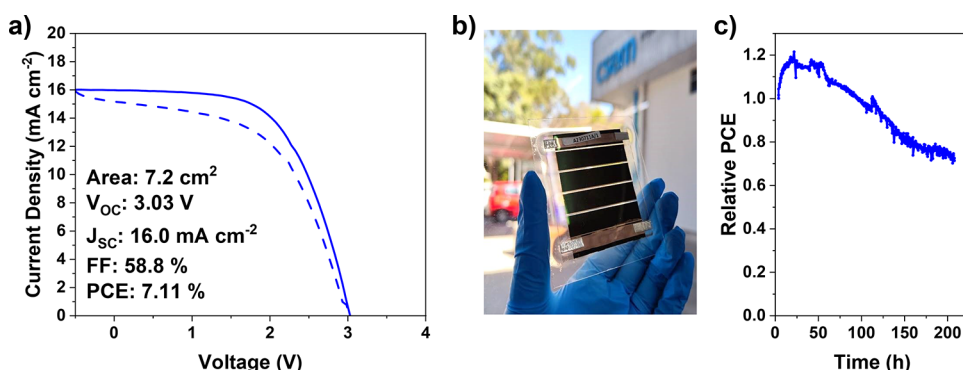


Figure 6. (a) JV curve of the champion minimodule of the structure PET/ITO/NiO_x/MeO-2PACz/perovskite/SnO₂ (1.25 wt %)/PC₆₁BM/BCP/Ag, (b) photograph of a typical encapsulated minimodule, and (c) stability of an encapsulated minimodule in air under 1 Sun illumination and MPPT conditions.

electrons at the surface of the samples, as expected for this sample architecture.³⁶ The turn off response of all samples is biphasic with a fast initial decay close to the time scale of the measurement resolution (0.5 s), followed by a slow decay on the 10–100 s time scale. The fast phase is attributed to the fast relaxation of photogenerated charge carriers, in this case through recombination of charges across the perovskite/PC₆₁BM interface.³⁶ The slow phase is related to the slow recombination of trapped charge carriers and the slow migration of ions in the perovskite layer.^{36–39}

The amplitude of the fast decay is much greater in the SnO₂ modified sample, indicating more complete fast relaxation of charges. This is consistent with the SnO₂ providing more conductive pathways for charges to recombine following the removal of the light bias. In contrast, in the Al₂O₃ modified sample, a greater fraction of the charge remains trapped in the PC₆₁BM layer leading to a reduction in the amplitude of the fast phase. This could be a result of the insulating nature of the Al₂O₃ nanoparticles slowing the rate of electrons in the PC₆₁BM recombining with holes in the perovskite, which is consistent with its charge blocking characteristics in device. Figure S16 gives the results of taking the first derivative of the SPV decays of the samples under study. As can be seen all samples show steep decays in the short time scales but equilibrate to similar slow rates of decay at longer time scales. This is consistent with the slow detrapping of charges and redistribution of ions in the perovskite layer discussed in previous work occurring by the same mechanisms in all samples.^{36,40}

Demonstration of Minimodules

Finally, to demonstrate the utility of this approach to large scale manufacturing we fabricated minimodules incorporating an SnO₂ nanoparticle interlayer (Figure 6). In this scenario we found a much higher nanoparticle concentration of 1.25 wt % to be optimum, with similar results also achieved with concentrations of 0.625 and 0.75 wt % (Figure S17). We attribute this difference to the PC₆₁BM needing to be near-defect free across the whole 7.2 cm² of the device for acceptable performance, rather than just 0.5 cm² for the previously discussed devices. No minimodules fabricated without a nanoparticle modified interface achieved current rectifying behavior. We further assessed the stability of the encapsulated modules by subjecting them to maximum power point tracking (MPPT) testing under 1 Sun illumination in ambient air (Figure 6c). The modules exhibit a T_{80} of

approximately 150 h (as measured from the PCE at $T = 0$ h). The degradation is driven by changes in both the FF and J_{SC} , with the FF being primarily responsible for the ~20% increase in PCE over the first 24 h (Figure S18). Further work is being undertaken to understand the degradation mechanism of these devices.

CONCLUSIONS

In summary we have demonstrated that noncontinuous interlayers of metal oxide nanoparticles can act as an interfacial modifier in large area perovskite solar cells enabling printing of continuous and high quality PC₆₁BM ETLs. Addition of the nanoparticle interlayers prevents micron scale pinhole formation in the PC₆₁BM layer, significantly improving the performance and reproducibility of the perovskite solar cells. We further demonstrate the impact of the choice of nanoparticle, comparing insulating Al₂O₃ and semiconducting SnO₂ nanoparticles. We show that Al₂O₃ nanoparticles passivate the perovskite/PC₆₁BM interface but, despite a surface coverage of just 20%, also significantly hinder the extraction of charges to the PC₆₁BM ETL resulting in a loss of current. Replacement of Al₂O₃ with SnO₂ nanoparticles results in faster charge extraction to the ETL, producing a 24% increase in average J_{SC} and devices achieving PCEs of up to 11%. Finally, we demonstrated the utility of this approach with the fabrication of 7.2 cm² minimodules utilizing SnO₂ nanoparticle interlayers. This work highlights the importance of material selection for interfaces and presents a strategy for improving interface quality and manufacturing yield in large area printed perovskite solar cells.

METHODS

Solutions

NiO_x nanoparticle solution with initial concentration of 2.5 wt % was diluted in a 1:10 proportion in ethanol prior to use. MeO2-PACz (TCI) was diluted in ethanol to achieve a final concentration of 0.33 mg/mL. PbI₂ (TCI), formamidinium iodide (Sigma-Aldrich), CsI (Sigma-Aldrich) were weighted accordingly and dissolved in a DMF free, DMSO based solvent system with 4% L- α -phosphatidylcholine to achieve a Cs_{0.17}FA_{0.83}PbI₃ solution. Likewise, PbBr₂ (Sigma-Aldrich), CsBr (Sigma-Aldrich) and formamidinium bromide (Sigma-Aldrich) were diluted in the same solution to achieve a Cs_{0.17}FA_{0.83}PbBr₃ composition. Both solutions were left stirring overnight at 60 °C. One hour prior to use, the solutions were mixed to achieve a final composition of a Cs_{0.17}FA_{0.83}Pb(I_{0.83}Br_{0.17})₃. Al₂O₃ (Sigma-Aldrich, nanoparticles, <50 nm particle size (DLS), 20 wt % in isopropanol) and SnO₂ (Avantama, nanoparticles, 5 wt %

in isopropanol) suspensions were made up immediately prior to use by dilution with anhydrous IPA to the required concentration. PC₆₁BM (Nano-C, 99%) solutions were made up to 20 mg/mL in *o*-xylene and stirred overnight in an N₂ environment at 80 °C. Bathocuproine (BCP) solutions were made up to 0.5 mg/mL in IPA in an N₂ environment and stirred overnight at 40 °C.

Device Fabrication

All wet film processes were carried out in ambient air within a clean room with controlled humidity (40–50% RH). A 10 cm wide PET-based web coated with ITO (200 nm, 18 Ω/sq) was used as the substrate for device fabrication. The depositions were carried out in a cleanroom environment with controlled humidity. NiO_x nanoparticle suspension was slot-die coated at 40 °C with a web speed of 1 m/min, an ink flow rate of 0.50 mL/min. The resulting film was thermally annealed in an in-line convection oven at 120 °C. Subsequently, the SAM layer was deposited on top of the NiO_x under the same conditions. Perovskite slot-die coating was performed at 100 °C with a web speed of 0.5 m/min and an ink flow rate of 0.30 mL/min. Nitrogen gas quenching was applied to aid solvent removal and enhance crystallization. The film was then thermally annealed at 150 °C in an in-line convection oven. The final perovskite film thickness was approximately 500 nm.

~7 cm strips of the PET/ITO/NiO_x/Me4-PACz/perovskite film were cut for evaporation of C₆₀/BCP layers or blade coating of the Al₂O₃/SnO₂, PC₆₁BM and BCP layers. Al₂O₃ and SnO₂ layers were blade coated using an optimized gap height of 400 μm, blade speed of 5 mm/s and bed temperature of 50 °C; for details of this optimization we direct the reader to the [Supporting Information](#) file. PC₆₁BM and BCP films were blade coated using a gap height of 400 μm, blade speed of 10 mm/s and bed temperature of 60 °C. All blade coated layers were deposited from 70 μL of the respective solution per substrate (7 × 10 cm). For devices with C₆₀ ETLs 20 nm of C₆₀ and 5 nm of BCP were sequentially evaporated under ultrahigh vacuum. All devices were finished with a 100 nm Ag cathode deposited under ultrahigh vacuum, with a shadow mask defining a pixel area of 0.5 cm² each.

Devices were encapsulated in ambient air conditions using a flexible barrier film (WVTR 10⁻⁴ g/m² day) and a UV-curable epoxy-based adhesive in a roll-to-roll machine, reaching a final adhesive thickness of 30 μm. The encapsulation process is discussed in greater detail by Soares et al.⁴¹

For the fabrication of mini-modules, a web containing a mechanically defined P1 pattern was used as the substrate. All layers were deposited according to the methods set out for the smaller cells, apart from where specified in the main text. After the deposition of BCP, a 532 nm laser with a fluence of 145 mJ/cm² was employed to selectively remove the layers and expose the bare ITO surface, thereby creating the P2 cut. Following the deposition of the silver cathode, the same laser was used at a reduced fluence of 29 mJ/cm² to remove the metal layer, thus creating the P3 pattern.

Characterization of PSCs

Current density–voltage (JV) curves were collected using a Keithley 2400 with the device exposed to 1 Sun illumination (Wacom WXS-156S-10 Solar Simulator) under flowing N₂. A scan speed of 0.5 V/s was used, with the devices being first being scanned in the reverse direction from rest before being allowed to return to rest and scanned in the forward direction. To avoid previously reported light-soaking effects,³⁴ devices were first soaked for 2 min under open circuit conditions before testing was carried out. Series resistances were calculated from the gradient of the device JV curve under 1 Sun around V_{OC} and the shunt resistances were calculated from the gradient of the device JV curve in the dark around 0 V.

Stability measurements were carried out using a custom LED solar simulator with an intensity of 1000 W m⁻² and approximate AM1.5G spectral match. Encapsulated devices were tested in air and held under MPP conditions for the duration of the test.

External quantum efficiency measurements were carried out using a Scientech PTS-2-QE/ICPE.

Scanning Electron Microscopy

Samples were mounted onto SEM stubs using carbon tape, and the edges were painted with silver paint to improve electrical contact with the stub. Images were taken on a Zeiss Gemini Sigma 300 FEG SEM instrument operating at 5 kV, with a working distance ≈5.5 mm. Image analysis to quantify the surface coverage of the nanoparticles and PC₆₁BM was performed using ImageJ.⁴²

Raman Spectroscopy

Raman spectral maps were collected using a Renishaw inVia microscope in backscattering mode with the samples exposed to a flowing N₂ atmosphere. An Ar ion laser (wavelength: 457 nm) was used to excite the samples, with exposure times and laser power optimized to increase the signal-to-noise ratio. An in-built 100 nm resolution encoded stage was used to position the sample automatically to produce the spatial maps. No degradation of the samples was observed following exposure to the laser. Spectrometer calibration was performed using an Si reference sample.

Atomic Force Microscopy

AFM images were collected using a Park NX10 AFM in noncontact mode with Park silicon PPP-NCHR tips. The AFM was controlled using SmartScan software and the images analyzed using Gwyddion.

Confocal PL Microscopy

PL imaging of the films was performed using an inverted fluorescence microscope (IX71, Olympus) with air objective lens (UMPlanFl 100×/0.95, Olympus) and appropriate optical filters. The samples were excited at 420 nm using a supercontinuum laser (Fianium WhiteLase, with power of 3.22 W/cm²), and the signal was detected with an electron-multiplying (EM) charge-coupled device (CCD) camera (iXon, Andor Technology). For the spectral measurements, the PL signal was further dispersed by using an imaging spectrograph (CLP-50LD, Bunkou Keiki) placed before the EM-CCD camera.

Time-Resolved PL Spectroscopy

Transient photoluminescence (TRPL) measurements were collected using an Edinburgh Instruments FLS1000 fitted with a 405 nm excitation laser (6 mW cm⁻² at 2 MHz). A long pass filter (>455 nm) was fitted between the sample and the detector to reduce the impact of reflected excitation light.

Simulations

To perform the drift-diffusion simulations shown in [Figure 4](#), we used Driftfusion.³³ This software is designed to model the behavior of ordered semiconductor devices which contain up to two species of mobile ionic charge. Details of the treatment of the mobile ionic charge can be found in our previous works.^{43,44} To simulate the JV measurements, the devices were first allowed to stabilize under AM1.5G illumination at a forward bias of 1.1 V. Then the voltage was swept from 1.1 to -0.1 V at a scan rate of 10 mV s⁻¹.

■ ASSOCIATED CONTENT

SI Supporting Information

The Supporting Information is available free of charge at <https://pubs.acs.org/doi/10.1021/acsami.5c24295>.

Detailed device performance statistics, SEM images, Raman mapping data, AFM images, detailed device stability data, EQE spectra, photoluminescence spectra, and details of drift-diffusion simulations ([PDF](#))

■ AUTHOR INFORMATION

Corresponding Author

Ji-Seon Kim – *Department of Physics and Centre for Processable Electronics, Imperial College London, London SW7 2AZ, U.K.; Department of Chemistry, University of Oxford, Oxford OX1 3QZ, U.K.; Department of Physics, Ewha Womans University, Seoul 03760, Republic of Korea;*

orcid.org/0000-0003-4715-3656; Email: ji-seon.kim@imperial.ac.uk

Authors

Charlie Henderson – Department of Physics and Centre for Processable Electronics, Imperial College London, London SW7 2AZ, U.K.; Present Address: Department of Chemistry, University of Oxford, Oxford OX1 3QZ, U.K.; orcid.org/0000-0003-3060-5329

Adriano S. Marques – Oninn Centro de Inovações, 31035536 Belo Horizonte, MG, Brazil; orcid.org/0000-0002-7545-298X

Izabela S. Bicalho – Oninn Centro de Inovações, 31035536 Belo Horizonte, MG, Brazil

Lucy J. F. Hart – Department of Physics and Centre for Processable Electronics, Imperial College London, London SW7 2AZ, U.K.; Department of Chemistry and Centre for Processable Electronics, Imperial College London, London W12 0BZ, U.K.; orcid.org/0000-0002-6269-4672

Amy Monahan – Department of Materials, Department of Bioengineering and Institute of Biomedical Engineering, Imperial College London, London SW7 2AZ, U.K.

Katherine Stewart – Department of Physics and Centre for Processable Electronics, Imperial College London, London SW7 2AZ, U.K.

Koki Asano – Department of Materials Science and Engineering, School of Materials and Chemical Technology, Institute of Science Tokyo, Tokyo 152-8552, Japan

Tianhao Lan – Department of Physics and Centre for Processable Electronics, Imperial College London, London SW7 2AZ, U.K.

Martin Vacha – Department of Materials Science and Engineering, School of Materials and Chemical Technology, Institute of Science Tokyo, Tokyo 152-8552, Japan; orcid.org/0000-0002-5729-9774

Molly M. Stevens – Department of Materials, Department of Bioengineering and Institute of Biomedical Engineering, Imperial College London, London SW7 2AZ, U.K.; Department of Physiology, Anatomy and Genetics, Department of Engineering Science, Kavli Institute for Nanoscience Discovery, University of Oxford, Oxford OX1 3QU, U.K.; orcid.org/0000-0002-7335-266X

Piers R. F. Barnes – Department of Physics and Centre for Processable Electronics, Imperial College London, London SW7 2AZ, U.K.; orcid.org/0000-0002-7537-8759

Diego Bagnis – Oninn Centro de Inovações, 31035536 Belo Horizonte, MG, Brazil

Complete contact information is available at: <https://pubs.acs.org/10.1021/acsami.5c24295>

Author Contributions

C.H.: conceptualization, formal analysis, investigation, methodology, visualization, writing—original draft; A.S.M.: investigation, methodology, validation, writing—review and editing; I.S.B.: investigation, methodology, validation; L.J.F.H.: investigation, formal analysis, software, writing—review and editing; A.M.: investigation; K.S.: formal analysis, investigation, writing—review and editing, K.A.: investigation; T.L.: validation; M.V.: supervision; M.M.S.: supervision; P.R.F.B.: supervision, software, writing—review and editing; D.B.: conceptualization, funding acquisition, methodology, supervision, writing—review and editing; J.-S.K.: conceptualization,

funding acquisition, project administration, supervision, writing—review and editing.

Notes

The authors declare the following competing financial interest(s): M.M.S. has invested in, consults for (or is on scientific advisory boards or boards of directors) and conducts sponsored research funded by companies related to the biomaterials field; has filed patent applications related to biomaterials; and has co-founded companies in the biomaterials field.

ACKNOWLEDGMENTS

This research was supported by the EPSRC ATIP Programme Grant (EP/T028513/1) and Petróleo Brasileiro S.A. (PETROBRAS) (2024/00334-0-ANP). C.H. acknowledges the UK EPSRC for DTP studentship and Oninn for CASE studentship support and for hosting a portion of this research in their laboratories during a placement. A.M. acknowledges the EPSRC and SFI Centre for Doctoral Training in Advanced Characterization of Materials (EP/S023259/1) and the Harvey Flowers Electron Microscopy Suite, Department of Materials, Imperial College London for provision of microscopy facilities. M.V. acknowledges JSPS KAKENHI grant number 23H04875 in Grant-in-Aid for Transformative Research Areas ‘Materials Science of Meso-Hierarchy.’ J.-S.K. thanks the Ewha Global Excellence Program. M.M.S. acknowledges funding from the Department of Science, Innovation and Technology (DSIT) and the Royal Academy of Engineering under the Chair in Emerging Technologies programme (CiET2021\94) and the University of Oxford Strategic Research Fund. The authors thank Fernanda Guimarães and Bárbara Miranda for their contributions to device fabrication and Gabriela Amorim for her contributions to the stability measurements.

REFERENCES

- (1) Chen, H.; Liu, C.; Xu, J.; Maxwell, A.; Zhou, W.; Yang, Y.; Zhou, Q.; Bati, A. S. R.; Wan, H.; Wang, Z.; Zeng, L.; Wang, J.; Serles, P.; Liu, Y.; Teale, S.; Liu, Y.; Saidaminov, M. I.; Li, M.; Rolston, N.; Hoogland, S.; Filleter, T.; Kanatzidis, M. G.; Chen, B.; Ning, Z.; Sargent, E. H. Improved Charge Extraction in Inverted Perovskite Solar Cells with Dual-Site-Binding Ligands. *Science* **2024**, *384* (6692), 189–193.
- (2) Song, F.; Zheng, D.; Feng, J.; Liu, J.; Ye, T.; Li, Z.; Wang, K.; Liu, S. F.; Yang, D. Mechanical Durability and Flexibility in Perovskite Photovoltaics: Advancements and Applications. *Adv. Mater.* **2024**, *36* (18), No. e2312041.
- (3) Jung, H. S.; Han, G. S.; Park, N.-G.; Ko, M. J. Flexible Perovskite Solar Cells. *Joule* **2019**, *3* (8), 1850–1880.
- (4) Park, N. G.; Zhu, K. Scalable Fabrication and Coating Methods for Perovskite Solar Cells and Solar Modules. *Nat. Rev. Mater.* **2020**, *5* (5), 333–350.
- (5) Weerasinghe, H. C.; Macadam, N.; Kim, J.-E.; Sutherland, L. J.; Angmo, D.; Ng, L. W. T.; Scully, A. D.; Glenn, F.; Chantler, R.; Chang, N. L.; Dehghanimadvar, M.; Shi, L.; Ho-Baillie, A. W. Y.; Egan, R.; Chesman, A. S. R.; Gao, M.; Jasieniak, J. J.; Hasan, T.; Vak, D. The First Demonstration of Entirely Roll-to-Roll Fabricated Perovskite Solar Cell Modules under Ambient Room Conditions. *Nat. Commun.* **2024**, *15* (1), 1656.
- (6) Wang, Y.; Duan, C.; Lv, P.; Ku, Z.; Lu, J.; Huang, F.; Cheng, Y.-B. Printing Strategies for Scaling-up Perovskite Solar Cells. *Natl. Sci. Rev.* **2021**, *8* (8), 1–24.
- (7) Uddin, M. A.; Rana, P. J. S.; Ni, Z.; Dai, X.; Yu, Z.; Shi, Z.; Jiao, H.; Huang, J. Blading of Conformal Electron-Transport Layers in p-i-n Perovskite Solar Cells. *Adv. Mater.* **2022**, *34* (30), 1–8.

- (8) Caprioglio, P.; Smith, J. A.; Oliver, R. D. J.; Dasgupta, A.; Choudhary, S.; Farrar, M. D.; Ramadan, A. J.; Lin, Y.; Christoforo, M. G.; Ball, J. M.; Diekmann, J.; Thiesbrummel, J.; Zaininger, K.; Shen, X.; Johnston, M. B.; Neher, D.; Stolterfoht, M.; Snaith, H. J. Open-Circuit and Short-Circuit Loss Management in Wide-Gap Perovskite p-i-n Solar Cells. *Nat. Commun.* **2023**, *14* (1), 932.
- (9) Küffner, J.; Wahl, T.; Schultes, M.; Hanisch, J.; Zillner, J.; Ahlswede, E.; Powalla, M. Nanoparticle Wetting Agent for Gas Stream-Assisted Blade-Coated Inverted Perovskite Solar Cells and Modules. *ACS Appl. Mater. Interfaces* **2020**, *12* (47), 52678–52690.
- (10) Cassella, E. J.; Oliver, R. D. J.; Thornber, T.; Tucker, S.; Goodwin, R.; Lidzey, D. G.; Ramadan, A. J. Alumina Nanoparticles Enable Optimal Spray-Coated Perovskite Thin Film Growth on Self-Assembled Monolayers for Efficient and Reproducible Photovoltaics. *J. Mater. Chem. C* **2024**, *12* (34), 13332–13342.
- (11) Perera, W. H. K.; Masteghin, M. G.; Shim, H.; Davies, J. D.; Ryan, J. L.; Hinder, S. J.; Yun, J. S.; Zhang, W.; Jayawardena, K. D. G. L.; Silva, S. R. P. Modification of Hydrophobic Self-Assembled Monolayers with Nanoparticles for Improved Wettability and Enhanced Carrier Lifetimes Over Large Areas in Perovskite Solar Cells. *Sol. RRL* **2023**, *7* (17), 1–11.
- (12) Jin, H.; Farrar, M. D.; Ball, J. M.; Dasgupta, A.; Caprioglio, P.; Narayanan, S.; Oliver, R. D. J.; Rombach, F. M.; Putland, B. W. J.; Johnston, M. B.; Snaith, H. J. Alumina Nanoparticle Interfacial Buffer Layer for Low-Bandgap Lead-Tin Perovskite Solar Cells. *Adv. Funct. Mater.* **2023**, *33* (35), 1–10.
- (13) Li, J.; Meng, X.; Huang, Z.; Dai, R.; Sheng, W.; Gong, C.; Tan, L.; Chen, Y. A Regularity-Based Fullerene Interfacial Layer for Efficient and Stable Perovskite Solar Cells via Blade-Coating. *Adv. Funct. Mater.* **2022**, *32* (1), 1–10.
- (14) Soares, G. de A.; Marques, A. dos S.; Guimarães, F. A.; Bicalho, I. S.; Fernandes, S. L.; Alves, G. X. G.; Pereira, D. C.; Miranda, B. H. de S.; Vilela, M. L. P.; Rodrigues, J. F.; Silva, T. M. G. da; Martins, J. L. da S.; Queiroz, R. V. de; Bagnis, D. Construção de um painel fotovoltaico flexível de perovskita. *Anais Congresso Brasileiro De Energia Solar - CBENS*, **2024**.
- (15) International Labour Organisation. ICSC 0084: *o-Xylene*. https://chemicalsafety.ilo.org/dyn/icsc/showcard.display?p_card_id=0084 (accessed 2026–01–21).
- (16) International Labour Organisation. ICSC 0642: *Chlorobenzene*. https://chemicalsafety.ilo.org/dyn/icsc/showcard.display?p_lang=en&p_card_id=0642&p_version=2 (accessed 2026–01–21).
- (17) Chung, K. T.; Reisner, J. H.; Campbell, E. R. Charging Phenomena in the Scanning Electron Microscopy of Conductor-Insulator Composites: A Tool for Composite Structural Analysis. *J. Appl. Phys.* **1983**, *54* (11), 6099–6112.
- (18) Dzwilewski, A.; Wågberg, T.; Edman, L. Photo-Induced and Resist-Free Imprint Patterning of Fullerene Materials for Use in Functional Electronics. *J. Am. Chem. Soc.* **2009**, *131* (11), 4006–4011.
- (19) Li, Z.; Wong, H. C.; Huang, Z.; Zhong, H.; Tan, C. H.; Tsoi, W. C.; Kim, J. S.; Durrant, J. R.; Cabral, J. T. Performance Enhancement of Fullerene-Based Solar Cells by Light Processing. *Nat. Commun.* **2013**, *4* (1), 2227.
- (20) Lee, M. M.; Teuscher, J.; Miyasaka, T.; Murakami, T. N.; Snaith, H. J. Efficient Hybrid Solar Cells Based on Meso-Superstructured Organometal Halide Perovskites. *Science* **2012**, *338* (6107), 643–647.
- (21) Peng, W.; Mao, K.; Cai, F.; Meng, H.; Zhu, Z.; Li, T.; Yuan, S.; Xu, Z.; Feng, X.; Xu, J.; McGehee, M. D.; Xu, J. Reducing Nonradiative Recombination in Perovskite Solar Cells with a Porous Insulator Contact. *Science* **2023**, *379* (6633), 683–690.
- (22) Golubev, T.; Liu, D.; Lunt, R.; Duxbury, P. Understanding the Impact of C60 at the Interface of Perovskite Solar Cells via Drift-Diffusion Modeling. *AIP Adv.* **2019**, *9* (3), No. 035026.
- (23) Glück, N.; Hill, N. S.; Giza, M.; Hutter, E.; Grill, I.; Schlipf, J.; Bach, U.; Müller-Buschbaum, P.; Hartschuh, A.; Bein, T.; Savenije, T.; Docampo, P. The Balancing Act between High Electronic and Low Ionic Transport Influenced by Perovskite Grain Boundaries. *J. Mater. Chem. A* **2024**, *12* (19), 11635–11643.
- (24) Tress, W.; Petrich, A.; Hummert, M.; Hein, M.; Leo, K.; Riede, M. Imbalanced Mobilities Causing S-Shaped IV Curves in Planar Heterojunction Organic Solar Cells. *Appl. Phys. Lett.* **2011**, *98* (6), No. 063301.
- (25) Min, H.; Lee, D. Y.; Kim, J.; Kim, G.; Lee, K. S.; Kim, J.; Paik, M. J.; Kim, Y. K.; Kim, K. S.; Kim, M. G.; Shin, T. J.; Il Seok, S. Perovskite Solar Cells with Atomically Coherent Interlayers on SnO₂ Electrodes. *Nature* **2021**, *598* (7881), 444–450.
- (26) Almora, O.; Cabrera, C. I.; Garcia-Cerrillo, J.; Kirchartz, T.; Rau, U.; Brabec, C. J. Quantifying the Absorption Onset in the Quantum Efficiency of Emerging Photovoltaic Devices. *Adv. Energy Mater.* **2021**, *11* (16), 1–9.
- (27) Ramadan, A. J.; Oliver, R. D. J.; Johnston, M. B.; Snaith, H. J. Methylammonium-Free Wide-Bandgap Metal Halide Perovskites for Tandem Photovoltaics. *Nat. Rev. Mater.* **2023**, *8* (12), 822–838.
- (28) Du, T.; Xu, W.; Xu, S.; Ratnasingham, S. R.; Lin, C.-T.; Kim, J.; Briscoe, J.; McLachlan, M. A.; Durrant, J. R. Light-Intensity and Thickness Dependent Efficiency of Planar Perovskite Solar Cells: Charge Recombination versus Extraction. *J. Mater. Chem. C* **2020**, *8* (36), 12648–12655.
- (29) Min, L.; Zhou, Y.; Sun, H.; Guo, L.; Wang, M.; Cao, F.; Tian, W.; Li, L. Carrier Dynamic Identification Enables Wavelength and Intensity Sensitivity in Perovskite Photodetectors. *Light Sci. Appl.* **2024**, *13* (1), 280.
- (30) Xu, W.; Du, T.; Sachs, M.; Macdonald, T. J.; Min, G.; Mohan, L.; Stewart, K.; Lin, C. T.; Wu, J.; Pacalaj, R.; Haque, S. A.; McLachlan, M. A.; Durrant, J. R. Asymmetric Charge Carrier Transfer and Transport in Planar Lead Halide Perovskite Solar Cells. *Cell Reports Phys. Sci.* **2022**, *3* (5), No. 100890.
- (31) Péan, E. V.; Dimitrov, S.; De Castro, C. S.; Davies, M. L. Interpreting Time-Resolved Photoluminescence of Perovskite Materials. *Phys. Chem. Chem. Phys.* **2020**, *22* (48), 28345–28358.
- (32) Chen, X.; Kamat, P. V.; Janáky, C.; Samu, G. F. Charge Transfer Kinetics in Halide Perovskites: On the Constraints of Time-Resolved Spectroscopy Measurements. *ACS Energy Lett.* **2024**, *9* (6), 3187–3203.
- (33) Calado, P.; Gelmetti, I.; Hilton, B.; Azzouzi, M.; Nelson, J.; Barnes, P. R. F. Driftfusion: An Open Source Code for Simulating Ordered Semiconductor Devices with Mixed Ionic-Electronic Conducting Materials in One-Dimension. *J. Comput. Electron.* **2020**, *21* (4), 960–991.
- (34) Henderson, C.; Luke, J.; Bicalho, I. S.; Correa, L.; Yang, E. J.; Rimmel, M.; Demetriou, H.; Chin, Y.; Lan, T.; Heutz, S.; Gasparini, N.; Heeney, M.; Bagnis, D.; Kim, J. Charge Transfer Complex Formation between Organic Interlayers Drives Light-Soaking in Large Area Perovskite Solar Cells. *Energy Environ. Sci.* **2023**, *16* (12), 5891–5903.
- (35) Di Girolamo, D.; Di Giacomo, F.; Matteocci, F.; Marrani, A. G.; Dini, D.; Abate, A. Progress, Highlights and Perspectives on NiO in Perovskite Photovoltaics. *Chem. Sci.* **2020**, *11* (30), 7746–7759.
- (36) Daboczi, M.; Hamilton, I.; Xu, S.; Luke, J.; Limbu, S.; Lee, J.; McLachlan, M. A.; Lee, K.; Durrant, J. R.; Baikie, I. D.; Kim, J.-S. Origin of Open-Circuit Voltage Losses in Perovskite Solar Cells Investigated by Surface Photovoltage Measurement. *ACS Appl. Mater. Interfaces* **2019**, *11* (50), 46808–46817.
- (37) Daboczi, M. *Origin of Charge Carrier Recombination Losses in Perovskite-Based Solar Cells Revealed by Interfacial Energetics and Surface Photovoltage*; Imperial College London, 2020.
- (38) Pockett, A.; Eperon, G. E.; Sakai, N.; Snaith, H. J.; Peter, L. M.; Cameron, P. J. Microseconds, Milliseconds and Seconds: Deconvoluting the Dynamic Behaviour of Planar Perovskite Solar Cells. *Phys. Chem. Chem. Phys.* **2017**, *19* (8), 5959–5970.
- (39) Leijtens, T.; Eperon, G. E.; Barker, A. J.; Grancini, G.; Zhang, W.; Ball, J. M.; Kandada, A. R. S.; Snaith, H. J.; Petrozza, A. Carrier Trapping and Recombination: The Role of Defect Physics in Enhancing the Open Circuit Voltage of Metal Halide Perovskite Solar Cells. *Energy Environ. Sci.* **2016**, *9* (11), 3472–3481.
- (40) Daboczi, M.; Ratnasingham, S. R.; Mohan, L.; Pu, C.; Hamilton, I.; Chin, Y.-C.; McLachlan, M. A.; Kim, J.-S. Optimal

Interfacial Band Bending Achieved by Fine Energy Level Tuning in Mixed-Halide Perovskite Solar Cells. *ACS Energy Lett.* **2021**, *6* (11), 3970–3981.

(41) Soares, G. A.; Bicalho, I. S.; Castro-Hermosa, S.; Corrêa, L. de Q.; Miranda, B. H. S.; Marques, A. dos S.; Fernandes, S. L.; Cunha, T.; de Freitas, V. V.; Vilaça, R. de Q.; Wouk, L.; Bagnis, D. A Comparative Study of Acrylic and Epoxy-Based Adhesives for Perovskite Solar Cells Encapsulation. *Sol. Energy* **2024**, *273*, No. 112496.

(42) Schneider, C. A.; Rasband, W. S.; Eliceiri, K. W. NIH Image to ImageJ: 25 Years of Image Analysis. *Nat. Methods* **2012**, *9* (7), 671–675.

(43) Xu, W.; Hart, L. J. F.; Moss, B.; Caprioglio, P.; Macdonald, T. J.; Furlan, F.; Panidi, J.; Oliver, R. D. J.; Pacalaj, R. A.; Heeney, M.; Gasparini, N.; Snaith, H. J.; Barnes, P. R. F.; Durrant, J. R. Impact of Interface Energetic Alignment and Mobile Ions on Charge Carrier Accumulation and Extraction in P-i-n Perovskite Solar Cells. *Adv. Energy Mater.* **2023**, *13* (36), 2301102.

(44) Hart, L. J. F.; Angus, F. J.; Li, Y.; Khaleed, A.; Calado, P.; Durrant, J. R.; Djurišić, A. B.; Docampo, P.; Barnes, P. R. F. More Is Different: Mobile Ions Improve the Design Tolerances of Perovskite Solar Cells. *Energy Environ. Sci.* **2024**, *17* (19), 7107–7118.